Effect of Electrode Structure on the Performance of Fully Printed Piezoelectric Energy Harvesters

Karem Lozano Montero, Mika-Matti Laurila, and Matti Mäntysalo, *Member, IEEE*

***Abstract*— Flexible piezoelectric energy harvesters have the potential to be used as power sources for wearable electronics. This study presents a simple printing-based fabrication process for a flexible piezoelectric energy-harvesting module with an integrated and optimized surface mount device (SMD)-based full-wave diode bridge rectifier. We investigate the effect of the electrode configuration on the energy-harvesting performance of the piezoelectric elements. Two types of piezoelectric elements are fabricated [a metal–insulator–metal (MIM) structure and an interdigitated electrode (IDE) structure] for comparison. The electrodes are inkjet printed using poly (3,4-ethylenedioxythiophene):poly(styrene sulfonate) (PEDOT: PSS), and the piezoelectric layer is bar-coated using poly (vinylidene-fluoride-co-trifluoroethylene) (P(VDF-TrFE)). The results show that a higher output power density can be obtained with the MIM-based energy harvester (7.8 μW/cm^3) when compared to the IDE-based harvester (20.8 nW/cm^3). Simulation results show that this is explained by the higher current output (i.e., charge generation ability) of the MIM-based structure.**

***Index Terms*— Energy harvester, flexible electronics, interdigitated, piezoelectric, printed electronics, poly(vinylidene-fluoride-co-trifluoroethylene) (P(VDF-TrFE)).**

I. Introduction

THE rapid advance of wearable electronics has enabled the development of devices with high flexibility, conformability, and ultralight weight with advanced functionalities for being used in a broad range of applications (e.g., biosignal monitoring, electronic textiles, and smarts watches) [1]–[5]. One of the main constraints when developing wearable electronics is the use of traditional bulky and rigid batteries as power sources due to their limitations on the miniaturization, portability, and flexibility of the wearable electronics [6], [7]. Therefore, it is required to study alternatives to enable the development of self-powered wearable devices without compromising their flexibility and conformability. Energy-harvesting techniques enable the use of self-powered devices by eliminating the need for recharging and replacing batteries. Different energy-harvesting mechanisms have been proposed as cost-effective solutions for the development of self-powered systems by harvesting energy from the environment, including mechanical energy harvesting, solar energy harvesting, thermal energy harvesting, and biochemical energy harvesting [8]. Among the different energy-harvesting mechanisms, mechanical energy harvesting has been widely studied owing to the abundant mechanical energy in the environment, especially by using mechanical energy harvesting based on piezoelectric elements [9]–[13]. Piezoelectric energy harvesters have the potential of being used as an energy source due to their straightforward fabrication and direct mechanical-to-electrical conversion capability [14].

Several piezoelectric energy harvesters have been reported in recent years [12], [15]–[19]. However, the fabrication methods utilized in these studies involve the use of multistep and complex fabrication methods (e.g., laser lift-off (LLO) [12], photolithography [16]), which results in time-consuming and expensive fabrication processes. Additive fabrication methods using highly scalable printed electronic technologies are a great alternative to simplify the fabrication process and reduce fabrication costs [20]. In most of the studies, the performance of the piezoelectric elements is characterized for energy-harvesting applications, however the design and integration of the rectifier circuit has not been studied for the most common piezoelectric element structures [i.e., metal–insulator–metal (MIM) structure and interdigitated electrode (IDE) structure]. Furthermore, there exists no direct performance comparison between harvesters utilizing the aforementioned electrode structures.

In this work, we study the performance of piezoelectric elements for energy-harvesting applications. Two types of electrode configurations were used for the fully printed piezoelectric elements: MIM and IDE. The piezoelectric element was integrated into a full-wave diode bridge rectifier to form a flexible piezoelectric energy-harvesting module. The energy-harvesting module was developed using a simple process based on additive fabrication technologies. The fabrication of the piezoelectric elements was done by inkjet printing the electrodes using the conductive polymeric ink poly(3,4-ethylenedioxythiophene):poly(styrene sulfonate) (PEDOT:PSS), whereas the piezoelectric polymer poly(vinylidene-fluoride-co-trifluoroethylene) (P(VDF-TrFE)) was bar-coated to form the electroactive layer. To minimize the power loss of the rectifying stage, we analyze the effect of the diode parameters when used with these types of piezoelectric elements.

Manuscript received December 29, 2021; revised February 15, 2022; accepted February 26, 2022. Date of publication March 2, 2022; date of current version April 6, 2022. This work was supported in part by the Academy of Finland under Grant 310618, in part by H2020 Marie Skłodowska-Curie Actions (MSCA) Individual Fellowship (IF) Grant UNOPIEZO under Grant 101022433, and in part by the Printed Intelligent Infrastructure–Finnish Research Infrastructure (PII-FIRI) under Grant 320019. The work of Karem Lozano Montero was supported by the Nokia Foundation. *(Corresponding author: Karem Lozano Montero.)*

The authors are with the Faculty of Information Technology and Communication Sciences, Tampere University, 33720 Tampere, Finland (e-mail: karem.lozanomontero@tuni.fi).

Digital Object Identifier 10.1109/JFLEX.2022.3156050

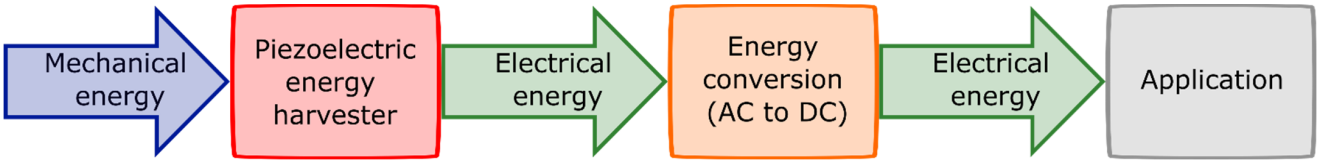

Fig. 1. Block diagram of a piezoelectric energy-harvester system showing its typical components.

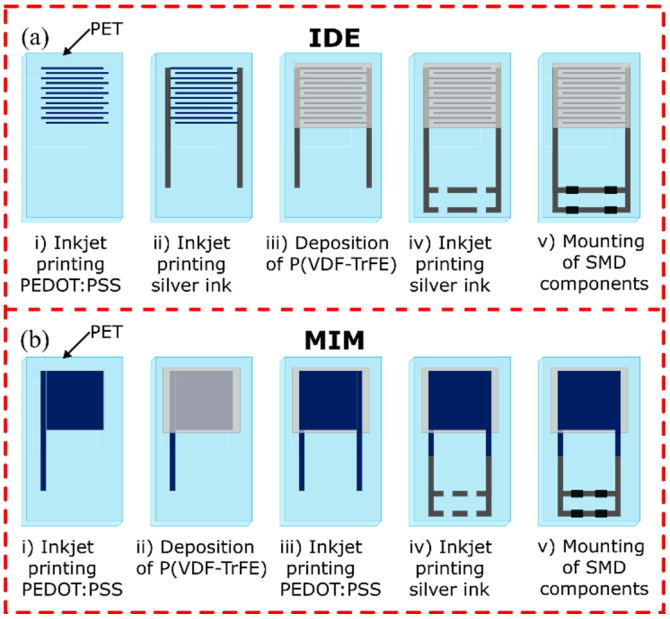

Fig. 2. Illustration of the fabrication of a piezoelectric energy harvester with the rectifier circuit integrated for (a) IDE and (b) MIM structures.

II. Materials and Methods

The schematic of an energy-harvesting system using piezoelectric components is shown in Fig. 1. The proposed energy-harvester module is composed of two main components: a fully printed piezoelectric element and a full-bridge rectifying circuit implemented with surface mount device (SMD) diodes. In this study, we analyze and compare the effect of two electrode configurations on the performance of the piezoelectric element: an MIM and IDE configuration. Volume-normalized power density is used as the comparison metric and because of this, similar thickness, and area IDE and MIM samples are fabricated. The fabrication process of each component is explained below.

A. Fabrication of Piezoelectric Energy Harvesters

1) Electrode Fabrication: The fabrication process of the piezoelectric energy harvesters is shown in Fig. 2. A polyethyleneterephalate (PET) foil (Melinex ST506, DuPont) with a thickness of 125 μm was used as the substrate. The bottom and top electrodes of the MIM-based piezoelectric energy harvester (15 mm $\times$ 15 mm) were inkjet-printed (DMP-2801, Fujifilm Dimatix) using PEDOT:PSS ink (Clevios P Jet 700, Heraeus) with the following printing parameters: a drop spacing of 30 μm, cartridge temperature of 38 °C, and stage at 45 °C. The printed structure was then annealed at 130 °C for 15 min in a convection oven. The IDE structure was also inkjet-printed (DMP-2801, Fujifilm Dimatix). First, the fingers were printed using PEDOT:PSS ink (Clevios P Jet 700, Heraeus) with the following printing parameters: a drop spacing of 40 μm, cartridge temperature of 38 °C, and stage at 45 °C. The fingers of the IDE structure were distributed over an area equal to the MIM-based elements. Two types of IDE structures were fabricated by varying the number of printed layers to form the electrode fingers (i.e., one and ten layers). This was followed by the printing of the current collectors with Ag-nanoparticle ink (DGP-40LT-15C, Advanced Nanoproducts) and the following printing parameters: 30-μm drop spacing, a cartridge temperature of 38 °C, and a stage temperature of 60 °C. The samples were then cured at 120 °C for 30 min in a convection oven.

2) Piezoelectric Layer: The deposition of the piezoelectric material P(VDF-TrFE) (FC Ink P, Arkema Piezotech) was done using an automatic bar-coater (Motorized Film Applicator CX4, MTV Messtechnik). The P(VDF-TrFE) layer was patterned using a polyimide (DuPont Kapton) mask, and the wet thickness of the printed layer was 60 μm. Then, the samples were annealed at 145 °C for 1 h in a convection oven. In the case of the MIM-based devices, the piezoelectric layer was deposited on top of the bottom electrode to form a sandwich-like structure PEDOT:PSS/P(VDF-TrFE)/PEDOT:PSS [Fig. 2(a)]. For the IDE-based devices, the piezoelectric layer was deposited on top of the interdigitated comb-like structure [Fig. 2(b)]. Previously, it has been reported that PEDOT:PSS films can be heated up to 200 °C without significantly affecting the conductivity [21]. Therefore, annealing the printed samples at 145 °C does not alter the properties of the bottom electrode or the substrate.

3) Poling: The poling process of the piezoelectric material was performed with a ferroelectric characterization tool (aixACCT TF2000, aixACCT Systems GmbH) coupled with a high-voltage amplifier (610C, TREK) while simultaneously measuring the polarization–electric field loop (P–E-loop) at room temperature. The poling field generated by the characterization tool was a triangular signal. The system generates a prepole signal followed by three bipolar signals. Each signal is followed by a 1-s relaxation time. The poling signal frequency was set to 2.5 Hz, and the duration of the poling process was approximately 5 s. The difference in the poling direction of the applied electric field is illustrated in Fig. 3 for the MIM and IDE structure. For the IDE structure, the electric field is determined as the applied voltage divided by the distance between consecutive electrodes G (see Fig. 3), and for the MIM structure, the distance between electrodes is determined by the piezoelectric layer thickness. The poling/P–E-loop

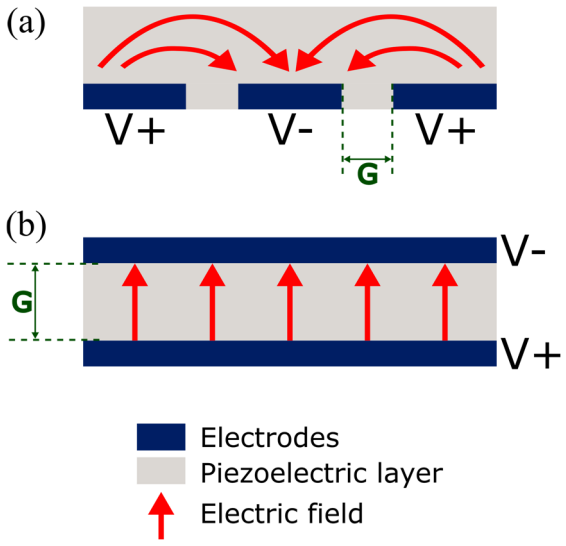

Fig. 3. Schematic of the poling orientation of the (a) IDE and (b) MIM devices in a cross sectional view. *G* represents the gap between electrodes.

measurement was repeated until the maximum remanent polarization (P_r) was achieved. The effective electrode area for the IDE-based devices was calculated using the method described previously in [22] and this value was used to determine the level of polarization. The chosen approach for effective area calculation has been previously used in [9] and [23]–[25].

4) Sensor Dimensions: For the IDE-based devices, the width of the electrode fingers and the gap width between the electrode fingers were measured using an optical microscope (BX60M, Olympus). The measurements were taken from three spots of the IDE structure. Additionally, the thickness of the P(VDF-TrFE) layer was measured using a stylus profilometer (Dektak XT, Bruker) for one sample of each sample set.

B. Flexible Piezoelectric Energy-Harvesting Module

A conventional full-wave bridge rectifier circuit was used to rectify the output voltage of the flexible piezoelectric energy harvester. The ac power generated by the piezoelectric element is converted to dc power, allowing the use of the piezoelectric device as a power source. The rectifier circuit layout was inkjet-printed using Ag-nanoparticle ink (DGP-40LT-15C, Advanced Nanoproducts) and the following printing parameters: 30-μm drop spacing, a cartridge temperature of 38 °C, and a stage temperature of 60 °C. The layout was printed on the same substrate as the piezoelectric energy harvester. The printed pattern was cured at 120 °C for 30 min. Then, SMD diodes and thin cables for measurement were mounted and fixed using silver epoxy (EPO-TEK H20E-PFC, Epoxy Technology) which was cured at 120 °C for 15 min. Finally, the module was encapsulated with a Parylene-C (GALXYL C, Galentis) layer approximately 800-nm thick using chemical vapor deposition (LabTop 3000, Para Tech Coating) to prevent the degradation of the printed circuits (especially PEDOT:PSS).

C. Electrical Characterization

The capacitance and resistance of the piezoelectric sensors were measured with a semiconductor analyzer (B1500A, Keysight). The open-circuit voltage of the piezoelectric energy harvesters was measured while applying uniaxial bending deformation with a sinusoidal dynamic force of 0.5 N at 1 Hz. To achieve this, the piezoelectric energy harvester was placed on a metal holder with a 20-mm distance between the supports facing downward. In the case of the IDE-based structure, the devices were placed so that the IDEs were in parallel to the bending axis. The sinusoidal dynamic force was applied using a setup composed of an electrodynamically actuated (Mini-Shaker Type 4810, Brüel and Kjaer) circular force probe (diameter 4 mm) with an integrated dynamic force reference sensor (209C02, PCB Piezotronics) and static force sensor (ELFS-T3E-20L Measurement Specialties Inc.). To induce uniaxial bending deformation, a cylindrical metal bar of 4 mm in diameter was placed between the circular force probe, and the device under measurement was clamped between the sample holder and the metal bar. The output of the piezoelectric energy harvester was connected to a commercial capacitor, and the voltage across the capacitor was monitored with a high-input-impedance unity-gain preamplifier connected to a digital oscilloscope (DSOX2002A, Keysight).

III. Results and Discussion

A. Optimization of the Rectifying Circuit

Piezoelectric energy-harvesting systems are a great alternative for scavenging energy as they can convert mechanical energy into electrical energy (Fig. 1). However, to use the generated energy as a power supply, an interface circuit is required. The purpose of this circuit is to act as an ac/dc converter as the electrical output of the piezoelectric element is ac. Usually, this circuit is composed of a rectifying stage (e.g., full-wave diode bridge) connected to an energy storage element (e.g., capacitor). The components used for the rectifier circuit play an important role in the performance of the circuit. There are two main constraints when using this type of configuration: 1) diode forward voltage (V_F) which decreases the maximum voltage across the capacitor when it is fully charged and 2) diode reverse leakage current (I_R) which may reduce the output power of energy-harvesting modules based on low-power nanogenerators [26], [27]. To select the components of the rectifying circuit in our study, first, we characterized the performance of a full-wave rectifier using different commercial diodes. The forward voltage and leakage current of these components is summarized in Table I. Additionally, in this experiment, four types of piezoelectric sensors were used to test the performance of the rectifying stage. A dynamic force was applied to the piezoelectric element using the setup described in Section III-C. Then, the piezoelectric element was connected to a full-wave bridge rectifier implemented with different components (see Table II), and a capacitor of 0.1 μF was connected at the output of the rectifier. The open-circuit voltage of the piezoelectric sensor (V_p) and the voltage across the capacitor (V_o) were measured to calculate the voltage drop of the rectifying stage. The voltage drop can be defined as

$$V_{drop} = V_p - V_o. \tag{1}$$

TABLE I
COMPONENT PARAMETERS ORDERED BY INCREASING REVERSE CURRENT. TYPICAL VALUES FROM THE DATASHEET AT 25 °C

Component	Type	V_f (@ I_f =100 mA)	I_R (@ V_R =5V)
PMEG120G10ELR	Silicon Germanium (SiGe) Rectifier	0.635 V	0.078 nA
PMEG6020ELR	Schottky rectifier	0.475 V	0.214 nA
1N4148	Standard diode	0.790 V	8.100 nA
1N4005	Standard diode	0.900 V	5000 nA[a]
STPS1L30	Schottky rectifier	0.395 V	6500 nA

[a] $V_R < 50$ V

TABLE II
MEASURED VOLTAGE DROP IN A FULL-WAVE BRIDGE RECTIFIER

Sensor structure	PMEG120G10ELR	PMEG6020ELR	STPS1L30	1N4005	1N4148
MIM[a]	0.06	0.26	1.37	0.10	0.23
MIM[b]	0.13	0.43	1.70	0.50	-[e]
MIM[c]	0.12	0.50	-[e]	0.28	0.30
IDE[d]	0.49	1.31	-[e]	0.72	1.03

[a] PZT, C_p (@1 kHz) = 6.63 nF
[b] Ag/P(VDF-TrFE)/PEDOT:PSS, C_p (@1 kHz) = 1.25 nF
[c] PEDOT:PSS/P(VDF-TrFE)/PEDOT:PSS, C_p (@1 kHz) = 0.44 nF
[d] PEDOT:PSS/P(VDF-TrFE), C_p (@1 kHz) = 0.032 nF
[e] Measured output voltage almost zero.

The voltage drop for each of the tested components and each of the different piezoelectric elements used in the experiment is listed in Table II. The lowest voltage drop was measured for the diode (PMEG120G10ELR) with the lowest reverse leakage current even though the forward voltage is not the lowest when compared to the other diodes used in this experiment. Furthermore, it also seems that the voltage drop over the rectifier is higher for the IDE-based piezoelectric energy harvester compared to the MIM-based elements. This indicates that the reverse leakage current of the diode is the dominant contributor to voltage drop with this type of harvester and that the internal impedance of the piezoelectric element should be considered when designing the rectifying stage. According to [26], low leakage current (i.e., reverse current) diodes are preferable for piezoelectric elements with low internal capacitance (<10 nF) which corresponds to the findings of this experiment. For example, when the component with the highest leakage current (STPS1L30) was used, the measured output voltage was almost zero for the piezoelectric component with the lowest internal capacitance. Therefore, the results of this experiment demonstrate that one of the limiting factors to reduce the voltage drop of the rectifying circuit is also the reverse leakage current of the selected diodes.

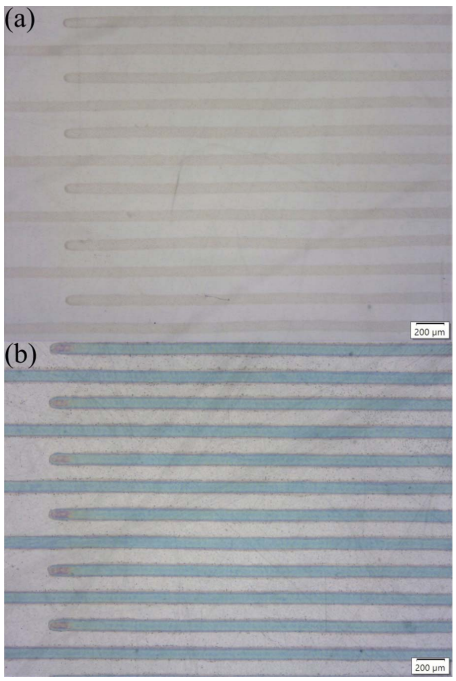

Fig. 4. Photograph of the printed IDE structures. (a) One-layer IDE. (b) Ten-layer IDE.

B. Comparison of MIM and IDE Energy Harvesters

1) Sample Description: The main parameters of the piezoelectric energy harvesters are listed in Table III. Each sample set contained four samples with the same thickness and area. However, the effective area of the MIM-based sensors is approximately four times the area of the IDE-based, and thus the charge generation with the MIM-based elements should be higher when compared to the IDE-based elements. The printed IDE structures are shown in Fig. 4. In both cases, the IDE structure was composed of 76 fingers. However, owing to the printing quality, the electrode finger width and the gap between the electrodes were different, and thus the IDE effective area varies from sample to sample. For one-layer IDE devices, the finger width was 87.0 ± 3.3 μm and the gap between fingers was 112.2 ± 4.7 μm, while for the ten-layer IDE devices,

TABLE III
PIEZOELECTRIC ENERGY HARVESTERS' PARAMETERS

Sensor structure	Number of samples	Piezoelectric layer thickness	Piezoelectric layer area	Electrode area[a] (mm^2)	Capacitance[b]	Resistance	Gap between electrodes
MIM	4	~4 μm	225 mm^2	225 mm^2	3.9 ± 0.1 nF	10.9 ± 7.8 GΩ	~4 μm[c]
IDE (1 layer)	4	~4 μm	225 mm^2	49 mm^2	25.1 ± 3.8 pF	154.7 ± 68.7 GΩ	112.2 ± 4.7 μm
IDE (10 layer)	4	~4 μm	225 mm^2	55 mm^2	22.7 ± 1.2 pF	164.3 ± 42.5 GΩ	103.4 ± 6.0 μm

[a] Electrode total interface area.
[b] Measured at 1 kHz.
[c] Corresponds to the piezoelectric layer thickness.

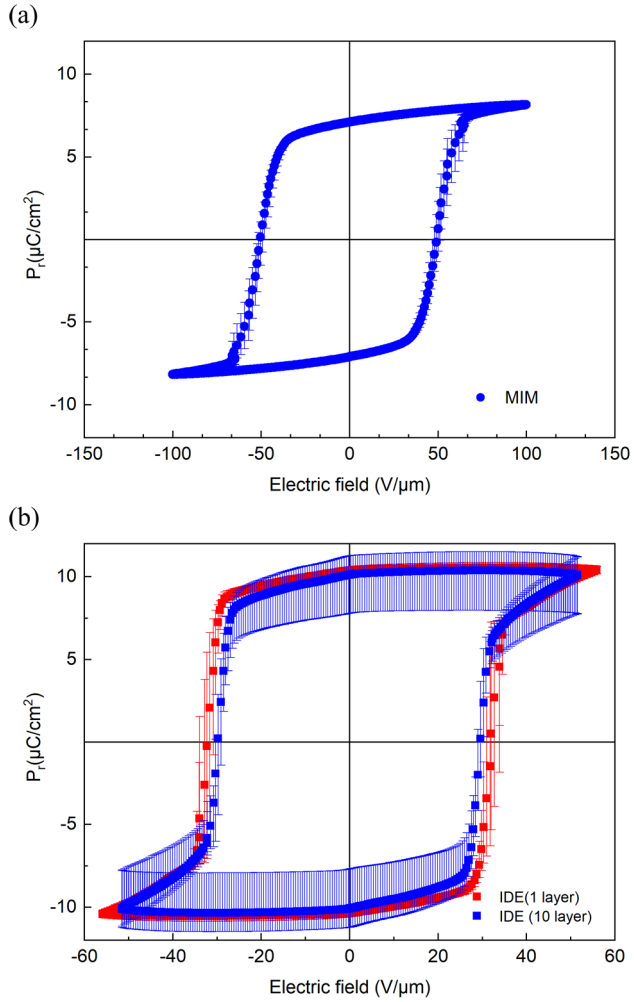

Fig. 5. P–E hysteresis loop. (a) MIM-based piezoelectric harvester. (b) IDE-based piezoelectric harvester (one- and ten-layer IDE structures). Error bars in the P–E loops show the minimum and maximum measured values.

the measured values were 97.5 ± 4.7 and 103.4 ± 6.0 μm, respectively. Additionally, the IDE-based devices showed a lower capacitance value when compared to the MIM-based devices, which may lead to a higher voltage sensitivity, despite the lower number of generated charges according to the equation

$$V = \frac{Q}{C} \tag{2}$$

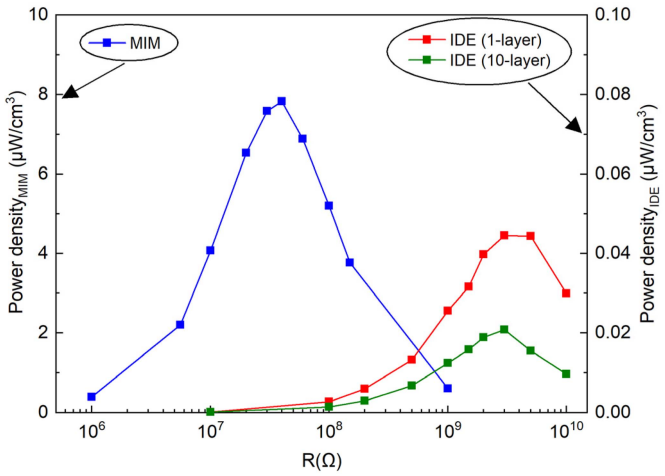

Fig. 6. Peak output power density of the MIM- and IDE-based elements.

where Q represents the number of charges generated by the piezoelectric energy harvester, C its capacitance, and V the corresponding output voltage.

2) Ferroelectric Performance: The P–E-loop was measured for each sensor structure to characterize their piezoelectric properties, which includes the remanent polarization (P_R) and the coercive field (E_c). The P–E-loop curves represent the polarization of the piezoelectric material while sweeping the applied electric field. In these measurements, the applied electric field (E) is determined by the equation

$$E = \frac{V}{G} \tag{3}$$

where V is the applied electric field and G is the distance between electrodes with opposite polarization. As shown in Fig. 3, for the MIM-based devices, G corresponds to the piezoelectric layer thickness, and for the IDE-based devices, it corresponds to the gap between electrode fingers. Fig. 5(a) and (b) shows the P–E-loop curve of the fabricated piezoelectric devices (MIM- and IDE-based). The plotted curve represents the average of four samples for each case, and the error bars represent the minimum and maximum measured values. In the MIM-based samples, the dipole alignment was saturated at ~100 V/μm. The average P_R value was 7.1 ± 0.1 μC/cm^2 and the average E_c was 49.3 ± 1.9 V/μm. For the IDE-based devices, the dipole alignment was saturated at ~50 V/μm. The average P_R value and the average E_c were

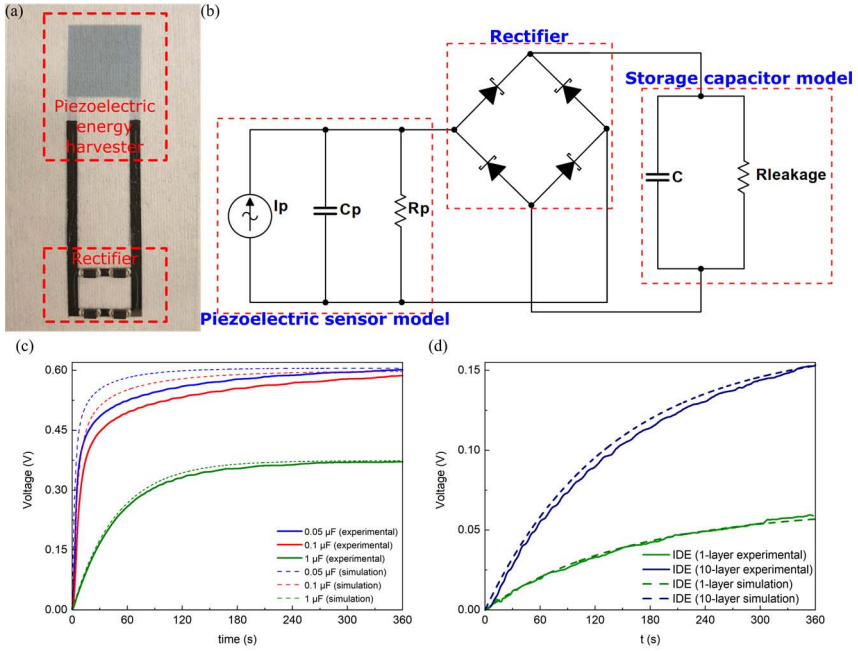

Fig. 7. (a) Photograph of one of the fabricated MIM-based piezoelectric energy-harvester modules. (b) Equivalent circuit of the module used for simulations. (c) Experimental and simulation results of a capacitor charging using an MIM-based piezoelectric nanogenerator for 0.05 μF ($R_{\text{leakage}} = 18$ GΩ), 0.1 μF ($R_{\text{leakage}} = 15$ GΩ), and 1 μF ($R_{\text{leakage}} = 200$ GΩ). (d) Experimental and simulation results of a capacitor charging using IDE-based piezoelectric nanogenerators for 0.05 μF.

10.3 ± 0.2 μC/cm^2 and 32.5 ± 1.3 V/μm, respectively, for the one-layer structures, while for the ten-layer structures, they were 10.1 ± 1.6 μC/cm^2 and 30.3 ± 0.5 V/μm, respectively. The IDE-based devices showed a higher P_{r} compared to the MIM-based devices. The observed difference may be related to the different poling direction distribution between the samples with IDE and MIM electrode configuration. Previous studies have also shown that the electrode area may have an impact on the remanent polarization [25], [28]. Thus, the observed difference may also result from the smaller electrode area of the IDE-based devices, which is ~4 times lower compared to the MIM-based devices (Table III).

3) Output Power Characterization: First, the output power of the piezoelectric sensors (i.e., MIM and IDE) was characterized without the rectifier. A mechanical excitation, which corresponds to a sinusoidal signal at 1 Hz, was applied to the sensors as described in Section II. A resistive load (R_{L}) was connected to the output of the sensor, and a load resistance sweep was done to determine the optimal resistive load to obtain the maximum harvested power. The resistive load was varied from 1 MΩ to 1 GΩ for the MIM-based sensors, and from 10 MΩ to 10 GΩ for the IDE-based sensors. The highest power density was achieved for a load resistor of 40 MΩ and 3 GΩ for the MIM- and IDE-based sensors, respectively. Fig. 6 shows the power dissipated by the load normalized by the piezoelectric layer volume. We can observe that the MIM-based piezoelectric harvester generates a higher output power when compared to the IDE-based piezoelectric harvester. The maximum power density of the MIM-based devices was 7.83 μW/cm^3. The IDE-based piezoelectric energy harvester printed with one layer showed a maximum power density of 44 nW/cm^3, while the ten-layer IDE-based device showed a maximum power density of 20.79 nW/cm^3. Thus, the energy-harvesting performance of the piezoelectric element utilizing the MIM electrode structure is far superior to that of a comparable (in thickness, area, and ferroelectric behavior) piezoelectric element with an IDE electrode structure.

C. Performance of the Piezoelectric Energy-Harvesting Module

To demonstrate the use of the piezoelectric elements as a power source, a piezoelectric energy-harvesting module [Fig. 7(a)] was used to charge capacitors with different values (0.05, 0.1, and 1 μF). The setup used for the power characterization was also used in this experiment. A sinusoidal dynamic force of 0.5 N with a frequency of 1 Hz was applied to the piezoelectric elements for mechanical deformation. The piezoelectric elements were characterized at low frequency (<10 Hz) to operate in the same frequency range of human motion [29]. Furthermore, the equivalent circuit of the energy-harvesting module [see Fig. 7(b)] was modeled to examine the effect of the different elements of the MIM- and IDE-based modules. In this model, the piezoelectric element is represented as a sinusoidal current source (I_{p}) connected in parallel to its internal resistance (R_{p}) and capacitance (C_{p}) [27], [30], [31]. The resistance and capacitance values were adjusted based on the electrical characterization of the piezoelectric elements. The peak current value was adjusted to obtain the experimentally determined open-circuit voltage of 1.6 V (peak–peak), which was achieved for 20.5 nA. Additionally, the leakage resistance of the storage

capacitor was also modeled. A SPICE model of the diode (PMEG120G10ELR) was used for simulations [32]. Fig. 7(c) shows the simulation results and experimental measurements of the voltage across the storage capacitor versus time during the charging process using an MIM-based energy-harvesting module. For the 0.05 and 0.1 μF capacitors, the voltage increases quickly at the beginning of the capacitor charging and reaches the saturation level approximately at the same rate as in the simulations. However, there is a small variation between the measured and the simulated output voltage, which can result from the difference between the ac signal generated by the piezoelectric sensor in the simulation compared to the ac signal generated in the experiments. The ac signal of the piezoelectric element is generated according to the applied force (amplitude and frequency), which may have small fluctuations during the measurement while in the simulations the ac signal is assumed to be constant. Furthermore, the saturation level of the 1-μF capacitor is lower compared to the 0.05 and 0.1 μF capacitors. By the characterization and simulation of the storage capacitor, it was found that the difference in the output voltage signals may be mostly associated with the leakage resistance of the capacitor. However, parasitic losses that are not considered in simulations may also have an impact on the charging rate of the capacitors.

The experimental characterization was also performed for the IDE-based energy-harvester modules; however, the generated energy was much lower compared to the MIM-based modules, and it was only possible to analyze the charging process of a 0.05-μF capacitor [see Fig. 7(c)]. The simulation analysis was done following the same procedure as for the MIM-based modules, which showed that the generated ac peak current was 80 and 155 pA for the one-layer IDE and ten-layer IDE, respectively. Thus, the ten-layer IDE generated approximately two times the ac current generated by the one-layer IDE. Previously, it has been shown that the conductivity of the electrodes has an impact on the generated power from the energy harvesters; the lower the sheet resistance, the higher the output current [33], [34]. In this study, the sheet resistance of the one-layer IDE was 1001.9 $\pm$ 86.7 Ω/sq, while for the ten-layer IDE, it was 562.3 $\pm$ 24.7 Ω/sq. Therefore, even though there was not a clear difference between IDE-based piezoelectric elements (i.e., one-layer and ten-layer) in the output power characterization (Section III-B), the conductivity of the electrodes plays an important role in power generation. Finally, the difference in the charging performance of the MIM- and IDE-based energy harvesters can be explained by the difference in the output current of the piezoelectric elements: although both elements are able to produce similar output voltage, the output current of the MIM-based element is much higher (in nanoampere range) compared to IDE output current (in picoampere range).

IV. Conclusion

We have fabricated and characterized piezoelectric energy-harvesting modules using two types of electrode structures for the piezoelectric elements. The design of our module consists of a flexible piezoelectric element integrated with a full-wave diode bridge rectifier. The piezoelectric elements are made of PEDOT:PSS and P(VDF:TrFE) forming an MIM-based configuration and an IDE-based configuration. The remanent polarization of the sensors was 7.1 $\pm$ 0.1 μC/cm^2 for the MIM-based, 10.3 $\pm$ 0.2 μC/cm^2 for the one-layer IDE-based, and 10.1 $\pm$ 1.6 μC/cm^2 for the ten-layer IDE-based configurations. The higher P_r of the IDE-based elements can be attributed to their smaller electrode area. By experimental analysis, we determined the importance of the diode selection for the rectifier when used with low internal capacitance piezoelectric elements, showing that the reverse leakage current of the diodes was the most limiting factor for decreasing the voltage loss of the modules. Before the integration of the piezoelectric element to the rectifier, the output power was characterized showing that the MIM-based piezoelectric elements can generate a higher instantaneous power compared to the IDE-based elements, which was 7.83 μW/cm^3. The performance of the piezoelectric energy-harvesting module was shown to be better for the MIM-based modules compared to the IDE-based modules. This is attributed to the higher current generation ability of the MIM-based structure, which may be in part affected by the lower electrode area and conductivity of the IDE-based structures.

References

[1] Y. Gu, T. Zhang, H. Chen, F. Wang, Y. Pu, C. Gao, and S. Li, "Mini review on flexible and wearable electronics for monitoring human health information," *Nanosc. Res. Lett.*, vol. 14, no. 1, p. 263, Dec. 2019.

[2] D. Dias and J. P. S. Cunha, "Wearable health devices—Vital sign monitoring, systems and technologies," *Sensors*, vol. 18, no. 8, p. 2414, Jul. 2018.

[3] S. Choi, H. Lee, R. Ghaffari, T. Hyeon, and D.-H. Kim, "Recent advances in flexible and stretchable bio-electronic devices integrated with nanomaterials," *Adv. Mater.*, vol. 28, no. 22, pp. 4203–4218, 2016.

[4] K. L. Montero *et al.*, "Self-powered, ultrathin, and transparent printed pressure sensor for biosignal monitoring," *ACS Appl. Electron. Mater.*, vol. 3, no. 10, pp. 4362–4375, Oct. 2021.

[5] R. Cao *et al.*, "Screen-printed washable electronic textiles as self-powered touch/gesture tribo-sensors for intelligent human–machine interaction," *ACS Nano*, vol. 12, no. 6, pp. 5190–5196, Jun. 2018.

[6] A. Ometov *et al.*, "A survey on wearable technology: History, state-of-the-art and current challenges," *Comput. Netw.*, vol. 193, Jul. 2021, Art. no. 108074.

[7] X. Fan *et al.*, "Flexible and wearable power sources for next-generation wearable electronics," *Batteries Supercaps*, vol. 3, no. 12, pp. 1262–1274, Dec. 2020.

[8] T. He, X. Guo, and C. Lee, "Flourishing energy harvesters for future body sensor network: From single to multiple energy sources," *iScience*, vol. 24, no. 1, Jan. 2021, Art. no. 101934.

[9] P. Schäffner *et al.*, "Microstructured single-layer electrodes embedded in P (VDF-TrFE) for flexible and self-powered direction-sensitive strain sensors," *Smart Mater. Struct.*, vol. 29, no. 8, p. 85040, 2020.

[10] Y. Cho *et al.*, "Enhanced energy harvesting based on surface morphology engineering of P(VDF-TrFE) film," *Nano Energy*, vol. 16, pp. 524–532, Sep. 2015.

[11] D. Chen, T. Sharma, Y. Chen, X. Fu, and J. X. J. Zhang, "Gold nanoparticles doped flexible PVDF-TrFE energy harvester," in *Proc. 8th Annu. IEEE Int. Conf. Nano/Micro Eng. Mol. Syst.*, Apr. 2013, pp. 669–672.

[12] J.-H. Kang, D. K. Jeong, and S.-W. Ryu, "Transparent, flexible piezoelectric nanogenerator based on GaN membrane using electrochemical lift-off," *ACS Appl. Mater. Interfaces*, vol. 9, no. 12, pp. 10637–10642, Mar. 2017.

[13] M. T. Todaro *et al.*, "Biocompatible, flexible, and compliant energy harvesters based on piezoelectric thin films," *IEEE Trans. Nanotechnol.*, vol. 17, no. 2, pp. 220–230, Mar. 2018.

[14] Z. Zhao, Y. Dai, S. X. Dou, and J. Liang, "Flexible nanogenerators for wearable electronic applications based on piezoelectric materials," *Mater. Today Energy*, vol. 20, Jun. 2021, Art. no. 100690.
[15] D. Wang, G. Yuan, G. Hao, and Y. Wang, "All-inorganic flexible piezoelectric energy harvester enabled by two-dimensional mica," *Nano Energy*, vol. 43, pp. 351–358, Jan. 2018.
[16] G.-T. Hwang *et al.*, "Self-powered wireless sensor node enabled by an aerosol-deposited PZT flexible energy harvester," *Adv. Energy Mater.*, vol. 6, no. 13, Jul. 2016, Art. no. 1600237.
[17] S. K. Ghosh, T. K. Sinha, B. Mahanty, and D. Mandal, "Self-poled efficient flexible 'ferroelectretic' nanogenerator: A new class of piezoelectric energy harvester," *Energy Technol.*, vol. 3, no. 12, pp. 1190–1197, Dec. 2015.
[18] S. Mondal, T. Paul, S. Maiti, B. K. Das, and K. K. Chattopadhyay, "Human motion interactive mechanical energy harvester based on all inorganic perovskite-PVDF," *Nano Energy*, vol. 74, Aug. 2020, Art. no. 104870.
[19] T. Park, B. Kim, Y. Kim, and E. Kim, "Highly conductive PEDOT electrodes for harvesting dynamic energy through piezoelectric conversion," *J. Mater. Chem. A*, vol. 2, no. 15, pp. 5462–5469, 2014.
[20] H. Wu, Y. Huang, F. Xu, Y. Duan, and Z. Yin, "Energy harvesters for wearable and stretchable electronics: From flexibility to stretchability," *Adv. Mater.*, vol. 28, no. 45, pp. 9881–9919, Dec. 2016.
[21] J. Huang, P. F. Miller, J. C. de Mello, A. J. de Mello, and D. D. C. Bradley, "Influence of thermal treatment on the conductivity and morphology of PEDOT/PSS films," *Synth. Met.*, vol. 139, no. 3, pp. 569–572, Oct. 2003.
[22] K. L. Montero, M.-M. Laurila, and M. Mäntysalo, "All printed flexible piezoelectric pressure sensor with interdigitated electrodes," in *Proc. IEEE 8th Electron. Syst.-Integr. Technol. Conf. (ESTC)*, Sep. 2020, pp. 1–6.
[23] F.-P. Zhang, J.-M. Du, Y.-S. Liu, and H.-L. He, "Inspection of remanent polarization in the ferroelectric ceramic PZT 95/5 through pyroelectric effect," *J. Amer. Ceram. Soc.*, vol. 90, no. 8, pp. 2639–2641, Aug. 2007.
[24] J. C. Hicks and T. E. Jones, "Frequency dependence of remanent polarization and the correlation of piezoelectric coefficients with remanent polarization in polyvinylidene fluoride," *Ferroelectrics*, vol. 32, no. 1, pp. 119–126, Jan. 1981.
[25] S.-B. Kim, H. Park, S.-H. Kim, H. C. Wikle, J.-H. Park, and D.-J. Kim, "Comparison of MEMS PZT cantilevers based on d_{31} and d_{33} modes for vibration energy harvesting," *J. Microelectromech. Syst.*, vol. 22, no. 1, pp. 26–33, Feb. 2013.
[26] K. Nadaud, G. Poulin-Vittrant, and D. Alquier, "Influence of topology and diode characteristics of AC-DC converters for low power piezoelectric energy harvesting," *Sens. Actuators A, Phys.*, vol. 330, Oct. 2021, Art. no. 112901.
[27] M. Edla, Y. Y. Lim, M. Deguchi, R. V. Padilla, and I. Izadgoshasb, "An improved self-powered H-bridge circuit for voltage rectification of piezoelectric energy harvesting system," *IEEE J. Electron Devices Soc.*, vol. 8, pp. 1050–1062, 2020.
[28] G. Han *et al.*, "Experimental investigation on the effect of top electrode diameter in PZT thick films," *Mater. Lett.*, vol. 65, no. 14, pp. 2193–2196, Jul. 2011.
[29] Y.-M. Choi, M. Lee, and Y. Jeon, "Wearable biomechanical energy harvesting technologies," *Energies*, vol. 10, no. 10, p. 1483, Sep. 2017.
[30] G. K. Ottman, H. F. Hofmann, A. C. Bhatt, and G. A. Lesieutre, "Adaptive piezoelectric energy harvesting circuit for wireless remote power supply," *IEEE Trans. Power Electron.*, vol. 17, no. 5, pp. 669–676, Sep. 2002.
[31] S. Du, Y. Jia, and A. A. Seshia, "Piezoelectric vibration energy harvesting: A connection configuration scheme to increase operational range and output power," *J. Intell. Mater. Syst. Struct.*, vol. 28, no. 14, pp. 1905–1915, Dec. 2016.
[32] NEXPERIA Germany GmbH. *PMEG120G10ELR (Spice Model)*. Accessed: Oct. 14, 2021. [Online]. Available: https://assets.nexperia.com/documents/spice-model/PMEG120G10ELR.txt
[33] B. Kumar and S.-W. Kim, "Recent advances in power generation through piezoelectric nanogenerators," *J. Mater. Chem.*, vol. 21, no. 47, pp. 18946–18958, 2011.
[34] C. Yang *et al.*, "Highly conductive liquid metal electrode based stretchable piezoelectric-enhanced triboelectric nanogenerator for harvesting irregular mechanical energy," *Mater. Des.*, vol. 201, Mar. 2021, Art. no. 109508.

Karem Lozano Montero received the M.Sc. degree in electrical engineering from Tampere University, Tampere, Finland, in 2019, where she is currently pursuing the D.Sc. (Tech.) degree with the Printable Electronics Research Group. Her doctoral research focuses on the development of ultrathin flexible printed sensors and energy harvesters for electronic skin applications.

Mika-Matti Laurila received the D.Sc. (Tech.) degree in electrical engineering from Tampere University, Tampere, Finland, in 2019.

He is currently working as a Marie Curie Research Fellow with Tampere University. His research interests are related to the development of fully printed, ultraflexible, and highly imperceptible piezoelectric sensors for biosignal monitoring.

Matti Mäntysalo (Member, IEEE) received the M.Sc. and D.Sc. (Tech.) degrees in electrical engineering from Tampere University of Technology, Tampere, Finland, in 2004 and 2008, respectively.

From 2011 to 2012, he was a Visiting Scientist with the iPack Vinn Excellence Center, School of Information and Communication Technology, KTH Royal Institute of Technology, Stockholm, Sweden. He is currently a Professor of electronics with Tampere University. He has authored or coauthored more than 100 research articles. His research interests include printed electronics materials, fabrication processes, stretchable electronics, sensors, and the integration of printed electronics with silicon-based technology (hybrid systems).

Dr. Mäntysalo has served IEEE EDS and EPS, IEC, and Organic Electronic Association. He was a recipient of the Academy Research Fellow (2015–2020) from the Academy of Finland. He has awarded for the first inkjet-printed global system for mobile communications (GSM)-based band integration.